7 Imaging Orbitals with X-rays

Liu Hao Tjeng
Max-Planck Institute for Chemical Physics of Solids
Nöthnitzer Str. 40, 01187 Dresden

Contents

E. Pavarini and E. Koch (eds.)
Orbital Physics in Correlated Matter
Modeling and Simulation Vol. 13
Forschungszentrum Jülich, 2023, ISBN 978-3-95806-689-2
http://www.cond-mat.de/events/correl23

1 Introduction

Strongly correlated materials show a wide variety of physical phenomena which include unconventional superconductivity, heavy fermion behavior, various forms of magnetism and multiferroicity, as well as colossal magneto-resistance and metal-insulator transitions. These materials usually contain transition-metal, rare-earth or actinide elements: the presence of the atomic-like d or f orbitals provides the degrees of freedom to generate those intriguing phenomena. Here the intricate interplay of band formation with the local correlation and atomic multiplet effects leads to phases that are nearly iso-energetic, making the materials properties highly tunable by doping, temperature, pressure or magnetic field. Understanding the behavior of the d and f electrons is therefor essential. The orbitals that actively participate in the formation of the ground state and low energy excitations need to be identified. So far, these orbitals have mostly been deduced from optical, x-ray and neutron spectroscopies in which spectra must be analyzed using theory or modelling. This, however, is also a challenge in itself, since *ab-initio* calculations hit their limits due to the many-body nature of the problem.

Here we developed a new experimental method that circumvents the need for involved analysis and instead provides the information as measured [1–3]. With this technique, we can make a direct image of the active orbital and determine what the actual atomic-like object looks like in the solid of interest. The method is based on non-resonant inelastic x-ray scattering (NIXS, also known as x-ray Raman scattering). Essential is that we involve an s core hole (s-NIXS) in the experiment as we will explain below. The transitions $s \rightarrow d$ and $s \rightarrow f$ are, however, dipole-forbidden, and therefore we have to utilize high momentum transfers in the inelastic scattering process so that the beyond-dipole terms gain spectral weight. In this chapter we will present the basic principles of s-NIXS and its experimental implementation. To demonstrate the strength of the technique, we will show how we can obtain the image of a textbook example, the $3d(x^2-y^2)(3z^2-r^2)$ hole orbital of the Ni^{2+} ion in a NiO single crystal [1]. We will also illustrate how s-NIXS can be used to directly identify the orbital character of excited states so that the relevant energy parameters which determine the low energy excitations can be extracted [3]. We will explain how s-NIXS can unveil covalency effects [3] and show the power of the direct-imaging capability of s-NIXS for the study of metallic systems where strong inter-site charge fluctuations hamper a reliable quantitative analysis of spectroscopic data.

2 Non-resonant inelastic scattering using an s core hole

The theoretical description of inelastic x-ray scattering can be found in a number of publications, see e.g. [4–7]. The double differential cross-section is the product of the Thomson photon cross section $\left(\frac{d\sigma}{d\Omega}\right)_{Tho}$ and the dynamical structure factor $S(\vec{q},\omega)$

$$\frac{d^2\sigma}{d\Omega d\omega} = \left(\frac{d\sigma}{d\Omega}\right)_{Tho} S(\vec{q},\omega). \tag{1}$$

The dynamical structure factor is a function of the scattering vector $\vec{q} = \vec{k_i} - \vec{k_f}$ and the energy loss $\omega = \omega_i - \omega_f$

$$S(\vec{q},\omega) = \sum_f \left|\left\langle f\left|e^{i\vec{q}\cdot\vec{r}}\right|i\right\rangle\right|^2 \delta(\hbar\omega_i - \hbar\omega_f - \hbar\omega). \quad (2)$$

Here i and f are the initial and final states. The transition operator $e^{i\vec{q}\cdot\vec{r}}$ can be expressed by its Taylor terms $1 + i\vec{q}\cdot\vec{r} + (i\vec{q}\cdot\vec{r})^2 + \cdots$, thereby showing directly that for small values of $|\vec{q}|$ the monopole and dipole transitions will dominate the signal while for large $|\vec{q}|$ values the beyond-dipole transitions will also contribute significantly. In our experiment, we will utilize excitations involving a core level. It is therefore useful to expand the transition operator $e^{i\vec{q}\cdot\vec{r}}$ in terms of semi-normalized (Racah's normalization) spherical harmonics $C^{\hat{q}^*}_{km}$ and $C^{\hat{r}}_{km}$. This results in a sum over spherical Bessel functions $j_k(\vec{q}\cdot\vec{r})$ and the wave functions can be factorized into a radial and angular part so that $S(\vec{q},\omega)$ can be written as

$$S(\vec{q},\omega) = \sum_f \left| \sum_k^{\infty} i^k (2k+1) \left\langle R_f \left| j_k(\vec{q}\cdot\vec{r}) \right| R_i \right\rangle \sum_{m=-k}^{k} \left\langle \phi_f \left| C^{\hat{q}^*}_{km} C^{\hat{r}}_{km} \right| \phi_i \right\rangle \right|^2 \delta(\hbar\omega_i - \hbar\omega_f - \hbar\omega)\,. \quad (3)$$

Not all terms in the above equation contribute to the sum. In fact, the non-zero terms are subject to the so-called triangle condition and parity selection rules

$$\left|l_f - l_i\right| \le k \le l_f + l_i \quad \text{and} \quad \left|l_f + l_i + k\right| = \text{even}, \quad (4)$$

where $l_i \rightarrow l_f$ labels the angular momenta in the transition. For example, a $d \rightarrow f$ transition has contributions only from terms with $k = 1$ (dipole), 3 (octupole), and 5 (triakontadipole). An $s \rightarrow d$ or $s \rightarrow f$ transition, on the other hand, has only one term each, namely $k = 2$ (quadrupole) or $k = 3$ (hexapole).

In the following we focus our attention to transitions involving an s core hole. Our particular interest originates from the fact that the s core hole is spherically symmetric. With the scattering vector $\vec{q}$ being the only quantity that determines the quantization axis, we can expect that the intensity of the transition will be determined by the hole density of the atomic-like final state in the direction of the scattering vector. In other words, we may expect that by rotating the atomic-like object while keeping the measurement geometry fixed, we can obtain an intensity profile that reflects the shape of the hole density of that object. A mathematical proof that the intensity profile is proportional to the hole density is given by Sundermann and Haverkort [8].

3 Experimental set-up

The s-NIXS measurements were performed at the High-Resolution Dynamics Beamline P01 of the PETRA-III synchrotron facility in Hamburg, Germany. Fig. 1 illustrates the experimental setup, showing the incoming beam $(\vec{k}_i, \omega_i)$, single crystal sample, scattered beam $(\vec{k}_f, \omega_f)$, and the corresponding momentum transfer vector $(\vec{q})$. The energy of the x-ray photon beam incident on the sample was tuned with a Si(311) double-reflection crystal monochromator (DCM). The photons scattered from the sample were collected and energy-analyzed by an array of twelve

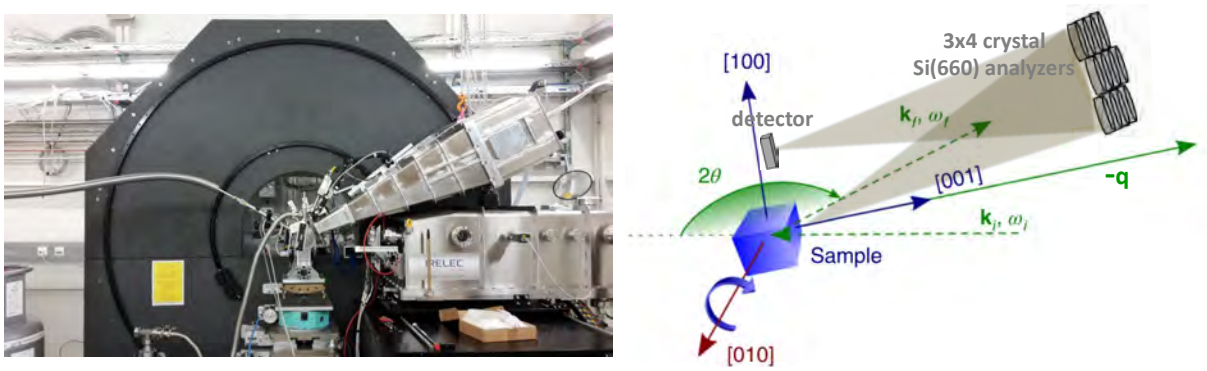

Fig. 1: *Experimental set-up and scattering geometry of the s-NIXS measurements at the P01 Beamline of the PETRA-III synchrotron facility in Hamburg, Germany. Schematic representation (right) from [1, 3].*

spherically bent Si(660) crystal analyzers. The analyzers are arranged in a 3×4 configuration. The energy of the analyzers ($\hbar\omega_f$) was fixed at 9690 eV; the energy loss spectra were measured by scanning the energy of the DCM ($\hbar\omega_i$). Each analyzer signal was individually recorded by a position-sensitive custom-made LAMBDA detector. The energy calibration was regularly checked by measuring the zero-energy-loss position of each spectrum. The best possible energy resolution was guaranteed by pixel-wise analysis of the detector recordings and measured as 0.7 eV (FWHM).

The positioning of the analyzer array determines the momentum transfer vector and the corresponding scattering triangle, which is defined by the incident and scattered photon momentum vectors, $\vec{k}_i$ and $\vec{k}_f$, respectively. The large scattering angle ($2\theta \approx 155°$) chosen for the current study assured a large momentum transfer of $|\vec{q}| = (9.6 \pm 0.1)\,\text{Å}^{-1}$ when averaged over all analyzers. $\vec{k}_f$ and 2θ were kept constant by fixing the energy and the position of the analyzer array. Since the energy transfer range of interest (100 to 120 eV) was small with respect to the incident and final energies (∼9700 eV), variation of $\vec{k}_i$ during energy scanning was insignificant. This guaranteed that the scattering triangle was virtually unchanged throughout the course of the experiment with $|\vec{q}| \approx$ constant.

The core of the experimental work is the measurement of $S(\vec{q}, \omega)$ as a function of the orientation of the single crystal sample with respect to the fixed experimental geometry as shown in Fig. 1. Here we define the sample angle φ as the angle between the fixed momentum transfer vector $\vec{q}$ and the single crystal surface normal.

4 Compton intensity and data treatment

To demonstrate the feasibility and accuracy of the s-NIXS method, we used a single crystal of NiO as a model system. It crystallizes in the rocksalt structure and is an antiferromagnetic insulator, with a well-understood high-spin Ni d^8 configuration. The measurements were carried out at 20 K in a He gas cryostat. The left panel of Fig. 2 shows a collection of NIXS spectra of a NiO single crystal measured for many different sample angles. The spectra show the sharp

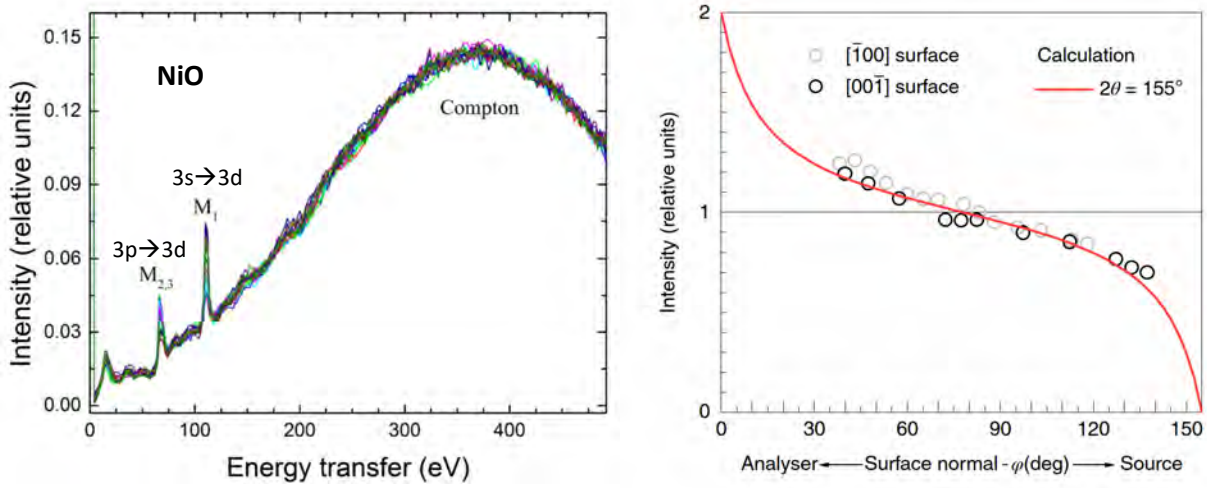

Fig. 2: *(left panel) Experimental NIXS spectra of NiO for a variety of crystal rotations φ with respect to the geometrically fixed momentum transfer vector $\vec{q}$. (right panel) Calculated and measured Compton intensity as function of sample angle φ with respect to specular geometry ($\varphi = 77.5°$) for a scattering angle $2\theta = 155°$. Reproduced from [1]*

$M_{2,3}$ edge ($3p \rightarrow 3d$) of nickel at around 70 eV and, important for the present study, the dipole-forbidden M_1 ($3s \rightarrow 3d$) excitations at around 110 eV. These features are on top of the broad Compton profile which peaks at about 350 eV energy transfer. The spectra are all normalized to this Compton signal.

We note that the line shape of the Compton profile does not change with angle. This is fully consistent with the fact that the scattering geometry is kept constant while rotating the sample. What does vary is the intensity of the Compton signal. This is related to how the x-rays are absorbed when entering the sample and when scattered out of the sample. This process can be modeled quantitatively since the NiO crystals used have well defined flat and shiny surfaces. The result of this modeling and the comparison with the experiment is displayed in the right panel of Fig. 2. The calculations were done for the actual scattering geometry of $2\theta = 155°$ so that for $\varphi = 77.5°$ specular geometry is fulfilled. Turning the sample towards (away from) the analyzer, increases (decreases) the intensity. One can observe a very good overall match between the experiment and the modeling. We thus can state that we understand fully the details of the scattering process, and in particular, that the intensity variations of the Compton profile is due to the absorption processes in the sample. We therefore can safely use the Compton profile to normalize our s-NIXS spectra.

To extract the M_1 edge intensities for further analysis, the Compton profile has been subtracted from each spectrum using a simple linear background.

5 Orientational dependence of the s-NIXS intensities

A close-up of the M_1 edge and its orientational dependence on $\vec{q} \parallel [001] - [101] - [100]$ is displayed in panel (a) of Fig. 3, and for $\vec{q} \parallel [001] - [111] - [110]$ in panels (b) and (c). The spectra consist of a single line and the line shape does not change with the angle. What does

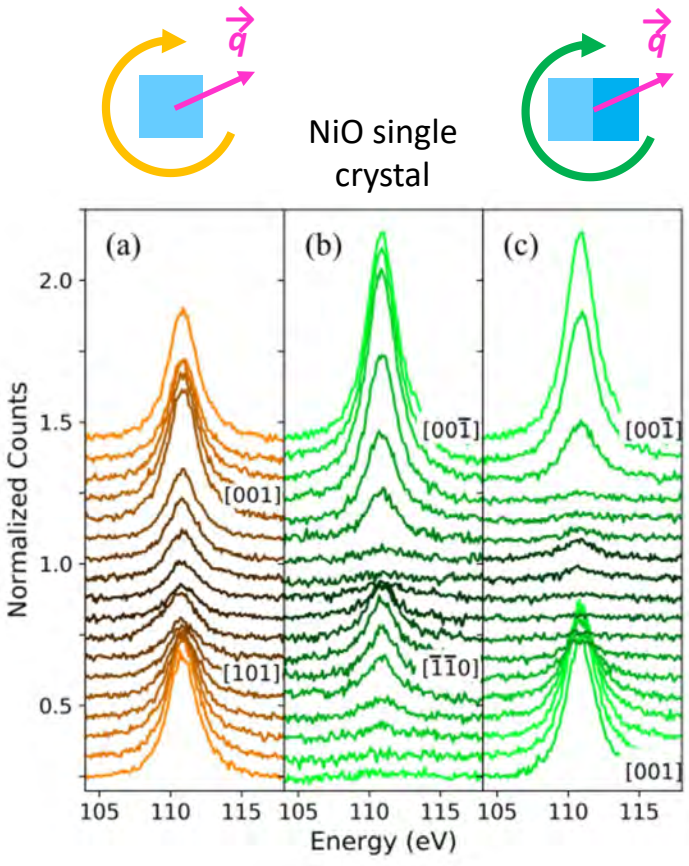

Fig. 3: *Stack of the Ni M_1 NIXS spectra acquired for $\vec{q}$ ∥ [001] – [101] – [100] (orange, panel a) and $\vec{q}$ ∥ [001] – [111] – [110] (green, panels b and c). Adapted from [1].*

change is the intensity. To quantitatively analyze these intensity variations, we determined the integrated intensity of each spectrum and placed it on a polar plot as displayed in the left and right panels of Fig. 4: the data points for $\vec{q}$ sweeping in the [001] – [101] – [100] plane are in orange, and for $\vec{q}$ in the [001] – [111] – [110] plane in green. They fall accurately on top of the orbital shapes which denote 'cuts' through the [001] – [101] – [100] (orange) and [001] – [111] – [110] (green) planes of the calculated three-dimensional orbital hole-density (square of the wave function) of the Ni high-spin $3d^8$ configuration in octahedral coordination, namely the $^3A_2$ $3d(x^2-y^2)3d(3z^2-r^2)$ as shown in the center panel of Fig. 4. This means that we indeed have generated a purely experimental method that can directly visualize the fundamental atomic-like quantum mechanical objects in solids. The information that we have obtained is extremely detailed; for example, we can clearly see the small lobes of the $3d(3z^2-r^2)$ contribution. We would like to remark that the $3d(x^2-y^2)$ contribution vanishes in the [001] – [111] – [110] plane, while both the $3d(x^2-y^2)$ and $3d(3z^2-r^2)$ contribute in the [001] – [101] – [100] plane. Here we note that we have used two orbital shapes in the inset in the right panel of Fig. 4: the blue dashed line is the $3d(x^2-y^2)3d(3z^2-r^2)$ function and the solid line is the same function convoluted with the angular acceptance of the 3×4 analyzers we used in our experiment. The near perfect agreement further demonstrates the accuracy of the method.

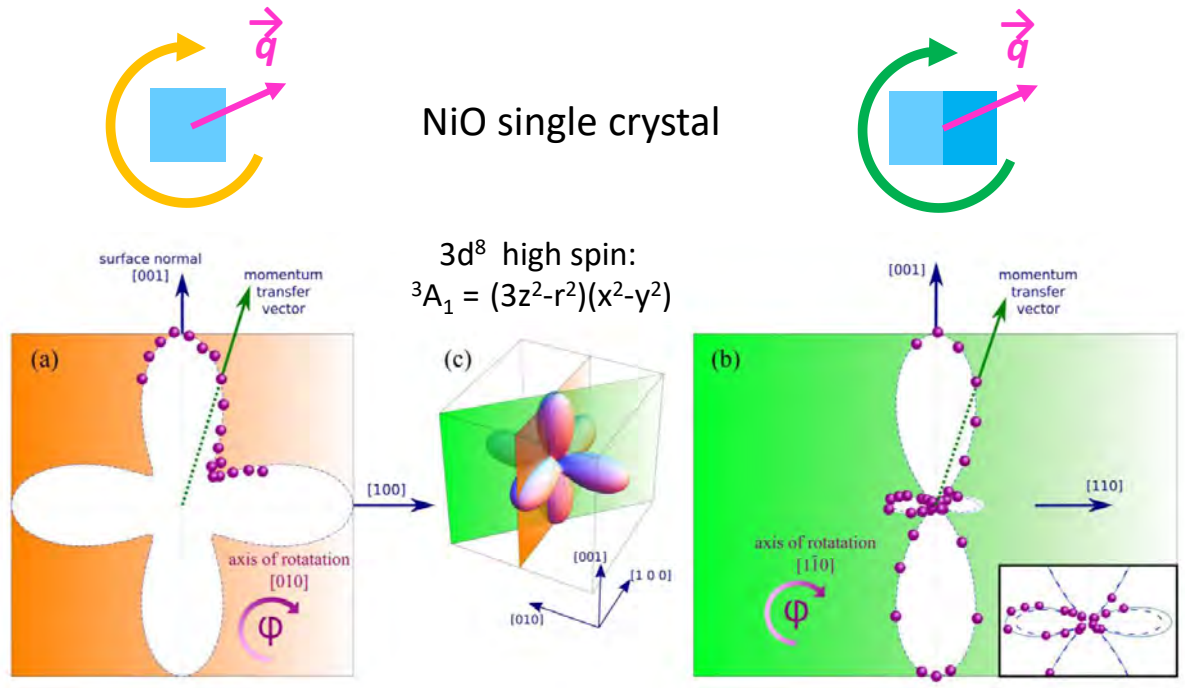

Fig. 4: *Left and right panels: polar plots of the integrated Ni M_1 intensities for $\vec{q}$ sweeping in the [001] – [101] – [100] plane (orange) and for $\vec{q}$ in the [001] – [111] – [110] plane (green). Central panel: theoretical three-dimensional orbital hole density of the Ni high-spin $3d^8$ configuration in octahedral coordination: ${}^3A_2$ $3d(x^2-y^2)3d(3z^2-r^2)$. Adapted from [1].*

6 Ground state properties

The orientational dependence of the integrated s-NIXS intensity at the Ni M_1 edge ($3s \rightarrow 3d$) directly maps the local orbital hole density of the ion in the ground state. There is no need to carry out a multiplet analysis of the spectral line shape to extract this information, in contrast to, for example, the non-s edges (e.g. $L_{2,3}(2p)$, $M_{2,3}$ $(3p)$, $M_{4,5}$ $(3d)$, $N_{4,5}$ $(4d)$, and $O_{4,5}$ $(5d)$) in both NIXS [5–7, 9–14] and XAS experiments [15–19]. The reason is fundamental: The M_1 $(3s \rightarrow 3d)$ quadrupolar excitation process involves a spherically symmetric s orbital, so the angular distribution of the intensity is solely determined by the hole charge distribution in the initial state with respect to the sole quantization axis which is given by the momentum transfer $\vec{q}$ [8]. This is similar to the dipole-allowed $s \rightarrow p$ transition in XAS, where an angular sweep of the polarization dependence maps out the orientation of the p hole directly.

We would like to emphasize that we do not need to perform complex configuration-interaction calculations to analyze or simulate the line shape of the spectra in order to obtain the local orbital hole density of the ion in the ground state. Details of the s-NIXS final states in fact do not matter because the information is extracted from the *integrated* intensity of the spectra (i.e., from the sum of the intensities of all final states). This can be understood as follows. Carrying out the energy integration of the dynamical structure factor $S(\vec{q},\omega)$ of Eq. (2), we obtain

$$\int S(\vec{q},\omega)\, d\omega = \sum_f \left|\langle f|e^{i\vec{q}\cdot\vec{r}}|i\rangle\right|^2 = \sum_f \langle i|e^{i\vec{q}\cdot\vec{r}}|f\rangle\langle f|e^{i\vec{q}\cdot\vec{r}}|i\rangle = \langle i|e^{i\vec{q}\cdot\vec{r}}e^{i\vec{q}\cdot\vec{r}}|i\rangle, \qquad (5)$$

where we have made use of the closure theorem $\sum_f |f\rangle\langle f| = 1$, assuming that the final states

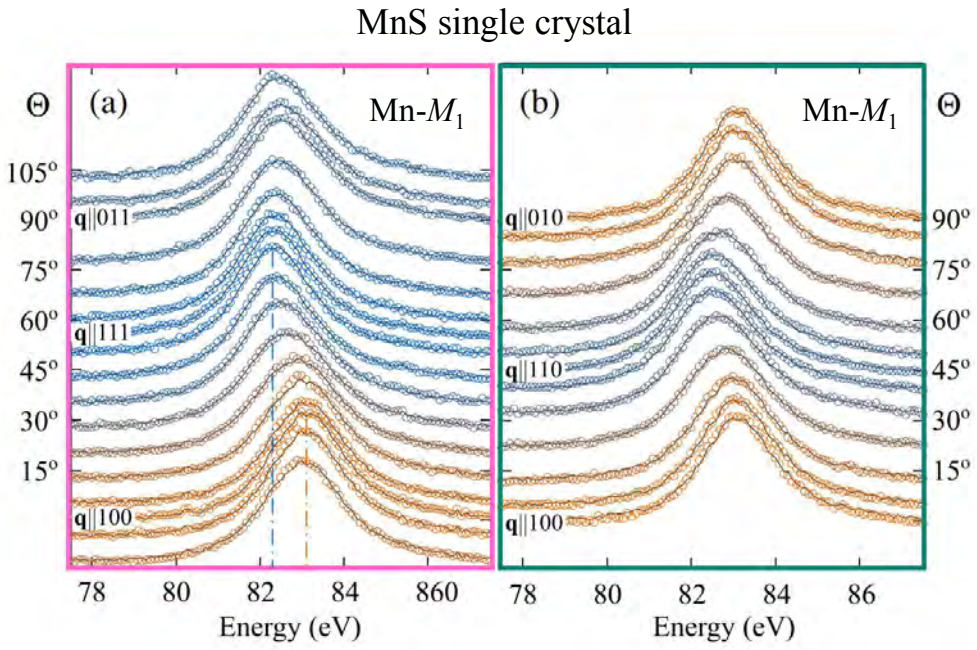

Fig. 5: *Stack of the Mn M_1 NIXS spectra acquired for $\vec{q}$ ∥ [100] – [111] – [011] (panel a) and [100] – [110] – [010] (panel b). The grey lines are the result of the fit procedure explained in the text. Reproduced from [3].*

$|f\rangle$ are complete. As a result, only the properties of the initial state are probed. Here we note that in this experiment we are considering only final states that can be reached in the $(s \rightarrow d)$ transition channel, so that what we have obtained is the d hole density in the initial state. This d hole density is a *locally* projected quantity since the final states carry the presence of the s core hole. The procedure is analogous to using linear and circular dichroism sum rules in x-ray absorption spectroscopies to extract expectation values of relevant quantum numbers of the system in the ground state [18, 20–22].

We would like to remark that the intensity distribution in s-NIXS is not what would be measured in an x-ray diffraction (XRD) experiment, even if such an experiment could be carried out with sufficient accuracy. In fact, s-NIXS provides information complementary to that from an XRD experiment by elucidating which local orbital or atomic wave function is active. The s-NIXS method presented here is not limited to ionic materials. In cases where configuration interaction effects play an important role due to covalency or itineracy, the image of the probed local orbital will reflect these effects directly as we will show below.

7 From ground state to excited states

Having established that s-NIXS is a powerful method for the investigation of the ground state, we will now explore the spectroscopy aspect of s-NIXS in order to study the excited states which are most often dominated by many-body atomic multiplet interactions in the d- and f-electron materials. In particular we aim to determine the orbital character of those states. The idea is that the use of an s core hole should simplify the analysis of the spectra in two significant

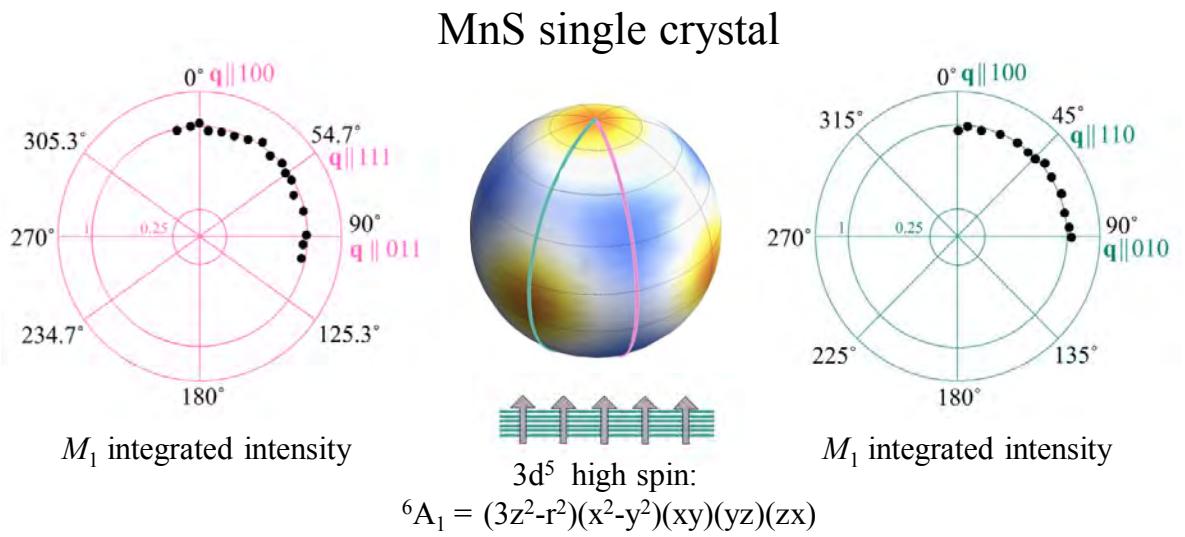

Fig. 6: *Left and right panels: polar plots of the integrated intensity of the Mn M_1 in the [100] – [111] – [011] plane (magenta) and in the [100] – [110] – [010] plane (dark cyan). Central panel: theoretical three-dimensional orbital hole density of the Mn high-spin $3d^5$ configuration in octahedral coordination: the spherical shaped ${}^6A_1$ $3d(x^2-y^2)(3z^2-r^2)(xy)(yz)(yz)$. Adapted from [3].*

aspects. First, the presence of the s hole does not add an extra orbital angular momentum so that use can be made of the well-established and readily available Sugano-Tanabe-Kamimura diagrams that depict the multiplet energy scheme of $3d$ ions for varying values of the crystal field [23]. Second, the identification of the orbital character of the multiplet state can be done in a direct manner by the imaging ability of the s-NIXS method. To exemplify these points, we have carried out the experiment on α-MnS, a rock salt type antiferromagnetic insulator with far from complete filling of the d shell so that orbital degrees of freedom are present in its excited states.

The α-MnS single crystal sample was grown by chemical vapor transport and during the measurements the sample was kept at a temperature of 50 K. The Mn M_1 edge spectra acquired at different angles are shown in panel (a) of Fig. 5 for the set $\vec{q} \parallel$ [100] – [111] – [011] and in panel (b) for $\vec{q} \parallel$ [100] – [110] – [010]. Also here the Compton contribution was used for normalization and has been subtracted from the spectra using a linear background. At first glance, there are no prominent variations in the peak intensities, but, as highlighted by the colors, the overall peak energy position varies as a function of angle, i.e., as a function the orientation of $\vec{q}$ with respect to the crystallographic axes.

Plotting first the integrated intensities as a function of angle in a polar plot, we indeed can observe from the left and right panels of Fig. 6 that there is essentially no orientational dependence, i.e., the hole charge density is constant in all directions. The spherical shape of the Mn $3d$ charge density as shown in the middle panel of Fig. 6 is fully consistent with the scenario in which all five spin-up or all five spin-down $3d$ orbitals are unoccupied, i.e., in which the Mn^{2+} $3d^5$ ion is in its Hund's rule high-spin ${}^6A_1$ ground state.

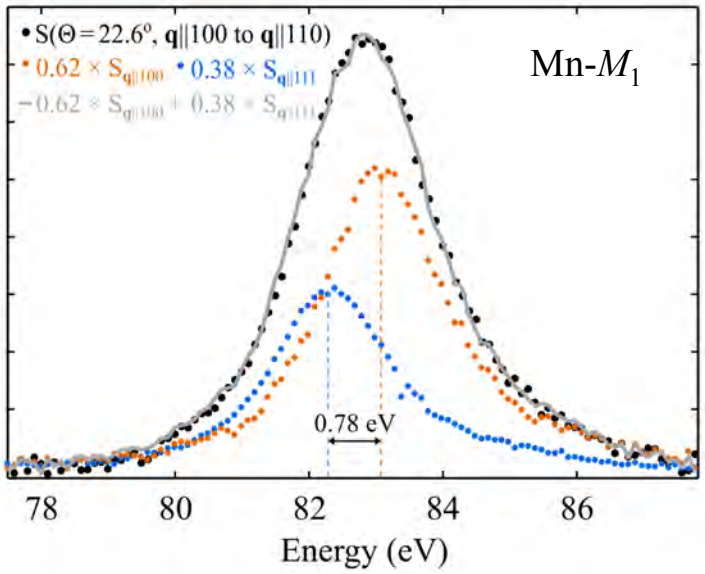

Fig. 7: *The experimental spectrum for a given angle Θ (black dots) is decomposed using the weighted sum of $\vec{q} \parallel$ [111] (blue dots) and $\vec{q} \parallel$ [100] (orange dots) spectra that provides the best fit (grey line). Reproduced from [3].*

8 Analysis of excited states

While the integrated intensity of the spectra is constant with angle, the energy position of the M_1 peak as displayed in panels (a) and (b) of Fig. 5 does vary with the orientation, between 82.37 eV (blue vertical line) for the $\vec{q} \parallel$ [111] spectrum and 83.15 eV (orange vertical line) for $\vec{q} \parallel$ [100]. Since no discernible dispersion can be expected for core-hole excitations, such a variation in energy indicates that the M_1 signal consists of features positioned at different energies whose relative intensities change with angle. With the Mn ion coordinated octahedrally by six S ions, we expect that the energy differences in the final states must be related to $10Dq$, the octahedral crystal field splitting between the t_{2g} and e_g orbitals.

We now assume that the two spectra acquired at $\vec{q} \parallel$ [111] and $\vec{q} \parallel$ [100], which show the extreme peak positions and narrowest line shapes, are the basic components making up the M_1 NIXS signal for every other orientation. We performed fits to all spectra using a linear combination of these two experimental spectra and determined their relative weights, so that each spectrum is described as $S(\Theta) = c_{111}(\Theta)S_{\mathbf{q}\parallel 111} + c_{100}(\Theta)S_{\mathbf{q}\parallel 100}$ where c_{111} and c_{100} are the free fitting parameters, as depicted in Fig. 7. The resulting fits are shown with gray lines in Fig. 5.

The weights $c_{111}(\Theta)$ and $c_{100}(\Theta)$ obtained by the fits are plotted in left panels Fig. 8 for the two sample orientations. We can observe that the angular dependence follows the shape of the t_{2g} and e_g states with great accuracy, allowing us to directly identify the orbitals reached in each excitation. In particular, the t_{2g} orbital shape is drawn by the angular dependence of $c_{111}(\Theta)$, the weight of the $S_{\vec{q}\parallel 111}$ component peaking at 82.37 eV. Likewise, the excitation into e_g orbitals is represented by $c_{100}(\Theta)$, the weight of the $S_{\vec{q}\parallel 100}$ component peaking at 83.15 eV. The difference between these two energies is due to the e_g-t_{2g} splitting, and it is therefore a direct measurement of the crystal field parameter $10Dq = 83.15\,\text{eV} - 82.37\,\text{eV} = 0.78\,\text{eV}$ as also illustrated in the right panel of Fig. 8.

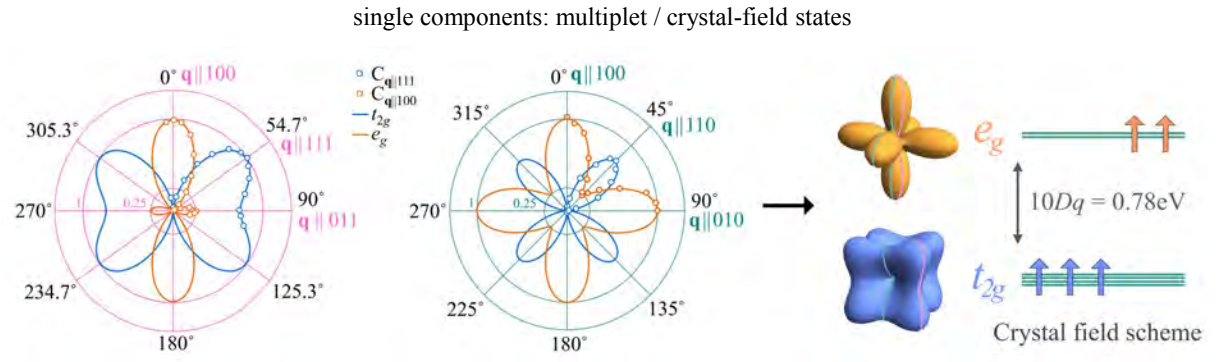

Fig. 8: *Left panels: the intensity of the $\vec{q} \parallel$ [100] (orange) and $\vec{q} \parallel$ [111] (blue) components follow the angular dependence of the e_g (orange) and t_{2g} (blue) orbitals, respectively. Right panels: The e_g-t_{2g} energy splitting is about $10Dq$ = 0.78 eV. Adapted from [3].*

9 Many-body energy-level diagram

A proper interpretation of the spectra must include the effects of Coulomb and exchange interactions between the electrons within the d shell, meaning that we need to put our results in a many body framework which takes into account both the full atomic multiplet theory and the local effect of the lattice. In particular, starting from the $3s^2 3d^5$ configuration for the ground state of the Mn ion in α-MnS, the s-NIXS process leads to a $3s^1 3d^6$ final state. Since the s core hole does not add an extra orbital angular momentum component, the multiplet structure of the final state will be closely related to the one of the $3d^6$ configuration. Therefore, one could make use of the well-established Sugano-Tanabe-Kamimura diagrams [23] for a quantitative analysis of s-NIXS spectra, after taking into account for some modifications due to the presence of the extra $3s$ spin. We exemplify this in Figs. 9 (a) and (b), where we reproduce the total energy diagrams for a Mn ion in $3d^6$ and $3s^1 3d^6$ configuration calculated with the *Quanty* code [24]. The corresponding Slater integrals F^2_{3d-3d} and F^4_{3d-3d} (and G^2_{3s-3d} for the $3s^1 3d^6$ configuration) have been obtained using the code by R.D. Cowan [25] and reduced to 80% of their Hartree-Fock value to account for configuration interaction effects not included in the calculation [16, 17].

To ease the comparison between the diagrams of the two configurations, the lowest energy state is not fixed at 0 eV for every $10Dq$ like it was done in the Sugano-Tanabe-Kamimura book [23]. Instead, the lowest state of the $3d^6$ configuration is put to zero only for $10Dq = 0$ eV, and serves as reference energy. In this way, the multiplets are split by the action of $10Dq$, but the average energy of the diagram is kept constant. The energy levels are labeled for zero crystal field ($10Dq = 0$ eV, spherical symmetry) with the ${}^{(2S_d+1)}L_d$ term symbols, where S_d and L_d represent the quantum numbers of the $3d$ shell and the orbital quantum numbers L_d are indicated with the usual letter notation (S, P, D, F, G...). The subscript in parenthesis indicates the degeneracy of each term symbol, also including the degeneracy given by the $3s$ hole. In total, the $3d^6$ configuration has $\binom{10}{6} = 210$ states, while $3s^1 3d^6$ has $2 \times \binom{10}{6} = 420$ states, due to the extra multiplicity of the $3s^1$ spin. The colors group the states in the diagrams according to their $3d$ spin multiplicity ($2S_d$+1): singlets are purple, triplets green, and quintets orange.

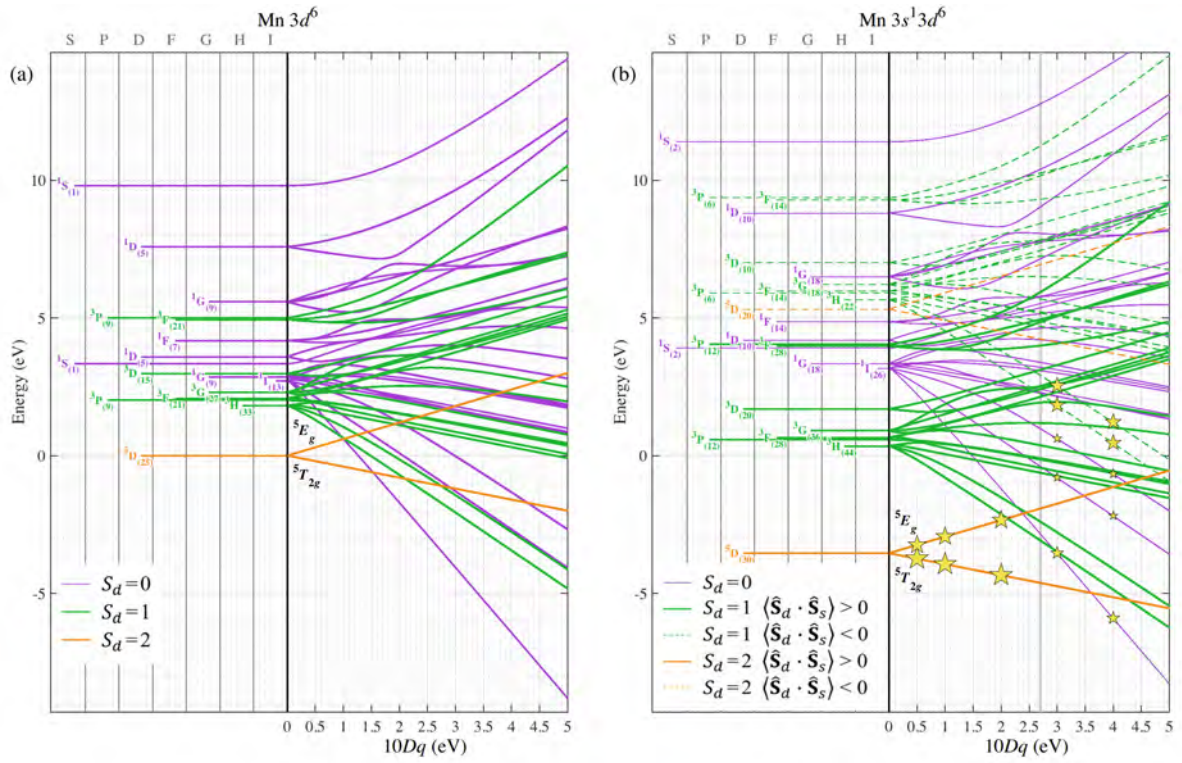

Fig. 9: *Modified Sugano-Tanabe-Kamimura diagrams showing the dependence on* $10Dq$ *of the energy levels of (a) Mn* $3d^6$ *(in absence of the core* $3s$ *hole) and of (b) Mn* $3s^1 3d^6$ *(the s-NIXS final state). Each multiplet is labeled with the corresponding term symbol at* $10Dq = 0$ *eV and in parenthesis its degeneracy. The colors indicate each state's spin multiplicity: purple for singlets, green for triplets and orange for quintets. In panel (b), the thick full lines represent the states having parallel* $\boldsymbol{S}_d$ *and* $\boldsymbol{S}_s$*, the thin dashed lines the states with* $\boldsymbol{S}_d$ *anti-parallel to* $\boldsymbol{S}_s$*, and the thin full lines the states not affected by* $\boldsymbol{S}_s$*. The stars indicate, for several* $10Dq$ *values, the possible final states of the s-NIXS process, and the vertical gray line at* $10Dq = 2.7$ *eV is the transition between the high and low spin configurations of the* $3d^5$ *ground state. Reproduced from [3].*

Starting from the singlets, it is straightforward to notice that the energy scheme within the set of singlets, as well as the dependence of each state on $10Dq$, is essentially the same between the two configurations $3d^6$ and $3s^1 3d^6$. This agrees with the fact that singlet states cannot be modified by an interaction with a $3s$ spin, given by $\langle \hat{\boldsymbol{S}}_d \cdot \hat{\boldsymbol{S}}_s \rangle$, which is zero for $S_d = 0$. The minor changes between the two groups ($\lesssim 10\%$ of the energy splittings) is due to the different values of the Slater integrals F^2_{3d-3d} and F^4_{3d-3d} between the two configurations. The sets of triplets (green lines) and quintets (orange) of the $3s^1 3d^6$ configuration, instead, are further divided in two subgroups depending on the relative alignment of $\boldsymbol{S}_d$ and $\boldsymbol{S}_s$. The states having the two spins parallel are represented with thick lines, while the thin dashed lines represent the states with opposite $\boldsymbol{S}_d$ and $\boldsymbol{S}_s$. These subgroups are each a replica of the corresponding $3d^6$ triplet or quintet set, rigidly shifted in energy due to the spin interaction.

To understand and predict these energy shifts due to the Coulomb interaction between the d electrons and the electron of the open $3s$ shell one can relate the Coulomb operator to the spin

		$S_{\text{tot}} = S_d + S_s$		$S_{\text{tot}} = S_d - S_s$	
S_d	$2S_d + 1$	$\langle \hat{\boldsymbol{S}}_d \cdot \hat{\boldsymbol{S}}_s \rangle$	$\Delta E\ [G^2_{3s-3d}]$	$\langle \hat{\boldsymbol{S}}_d \cdot \hat{\boldsymbol{S}}_s \rangle$	$\Delta E\ [G^2_{3s-3d}]$
0	1	0	0	0	0
$\frac{1}{2}$	2	$\frac{1}{4}$	$-\frac{1}{10}$	$-\frac{3}{4}$	$\frac{3}{10}$
1	3	$\frac{2}{4}$	$-\frac{2}{10}$	$-\frac{4}{4}$	$\frac{4}{10}$
$\frac{3}{2}$	4	$\frac{3}{4}$	$-\frac{3}{10}$	$-\frac{5}{4}$	$\frac{5}{10}$
2	5	$\frac{4}{4}$	$-\frac{4}{10}$	$-\frac{6}{4}$	$\frac{6}{10}$
$\frac{5}{2}$	6	$\frac{5}{4}$	$-\frac{5}{10}$	$-\frac{7}{4}$	$\frac{7}{10}$

Table 1: *Eigenvalues of $\hat{\boldsymbol{S}}_d \cdot \hat{\boldsymbol{S}}_s$, related to the energy splitting due to the Coulomb interaction of pure spin multiplets (i.e., neglecting spin-orbit interaction) in the d shell with the open $3s^1$ core shell for states with the d spin either parallel ($S_{tot} = S_d + S_s$) or anti-parallel ($S_{tot} = S_d - S_s$) to the core s spin. Reproduced from [3].*

operators of the d shell and s shell. We have

$$H^{\text{Coulomb}}_{3s-3d} = -\frac{2}{5}\hat{\mathbf{S}}_d \cdot \hat{\mathbf{S}}_s\, G^2_{3s-3d} + n_d\big(F^0_{3s-3d} - \frac{1}{10}G^2_{3s-3d}\big). \tag{6}$$

The last term in the equation is constant for all multiplets within a $3s^1\,3d^n$ configuration and as such does not lead to a splitting between the different states. The eigenvalues of $\hat{\boldsymbol{S}}_d \cdot \hat{\boldsymbol{S}}_s$ can be obtained simply by inverting the formula [26] $(\hat{\boldsymbol{S}}_{\text{tot}})^2 = (\hat{\boldsymbol{S}}_d)^2 + (\hat{\boldsymbol{S}}_s)^2 + 2\hat{\boldsymbol{S}}_d \cdot \hat{\boldsymbol{S}}_s$, where S_{tot} can be $S_d + S_s = S_d + \frac{1}{2}$ or $|S_d - S_s| = |S_d - \frac{1}{2}|$, and remembering that the eigenvalue of $(\hat{\boldsymbol{S}})^2$ is $S(S+1)$. The resulting eigenvalues are listed in Table 1 for each possible value of S_d.
Typical values of G^2_{3s-3d} for the $3d$ series, after a reduction to 80 % of their Hartree-Fock values, range from 8.5 to 10.2 eV. In general, ΔE is larger for larger spin multiplicities. With these ingredients, one can easily build the Sugano-Tanabe-Kamimura diagrams of the NIXS final configuration from the ones without the $3s$ core hole, listed, for example, in Figs. 5.1–5.7 of the famous book of S. Sugano, Y. Tanabe and H. Kamimura [23]. This allows the diagram of the possible s-NIXS final states to be reproduced without the need for performing new calculations and, by comparing the diagrams to the spectra, quantitatively determine the value $10Dq$.

10 Spectral lineshape

The next step towards a complete understanding of the s-NIXS spectra is to realize that not all states depicted in Fig. 9 (b) can be reached starting from the ground state of Mn^{2+} in α-MnS. In our case, the addition of one extra $3d$ electron ($s = 1/2$) to the high-spin $^6A_1$ ($S_d = 5/2$) ground state can only lead to quintet final states ($S_d = 2$), with the $3s^1$ spin parallel to the majority spin of the $3d$. Therefore, $-\frac{2}{5}G^2_{3s-3d}\,\langle \hat{\boldsymbol{S}}_d \cdot \hat{\boldsymbol{S}}_s \rangle < 0$, and the low energy replica of the quintet set is reached. The possible s-NIXS final states for different values of $10Dq$ are

indicated with stars in Fig. 9 (b), where the values of $10Dq$ corresponding to the initial $3d^5$ high-spin configuration ${}^6A_1$ are to the left of the gray vertical line, and low-spin on the right. The size of each star is proportional to the intensity of the corresponding peak on the s-NIXS spectra, averaged over the two sets of directions presented here (i.e., $\mathbf{q} \parallel$ [100] – [111] – [011] and $\mathbf{q} \parallel$ [100] – [110] – [010]). There are only two states in the diagrams that can be reached with a s-NIXS excitation, namely the ${}^5T_2$ (the extra $3d$ electron occupying t_{2g} orbitals) and ${}^5E$ (the extra electron in the e_g). From the shape of the final state orbitals as imaged in Fig. 8, we can identify immediately that the lower energy peak belongs to the ${}^5T_2$ state and the higher to the ${}^5E$. It is then straightforward to understand, as predicted above, that in our case the experimental peak energy separation of 0.78 eV corresponds one-to-one to the $10Dq$ value.
It is worth looking into Fig. 9 (b) in more detail. For $10Dq$ values on the right of the gray vertical line, the ground state will no longer be the high-spin but the low-spin $3d^5$. The consequence for the s-NIXS spectrum is dramatic. It switches from a two-peak structure (two stars) into a five-peak features (three small stars, two large stars). This demonstrates that the line shape of the s-NIXS spectrum is an extremely sensitive indicator of the ground state symmetry. The value of $10Dq$ can be determined directly from the spread of the five peaks. Consequently, the ground state hole density will also change in going from high to low-spin, i.e., from spherical ($t_{2g}^3 e_g^2$-like) to highly non-spherical (t_{2g}^5-like), which can be revealed directly by the image obtained from the directional dependence of the integrated s-NIXS intensity.

11 Covalency

We now investigate the influence of covalency on the s-NIXS image of the local d hole density and the spectra. To this end, we have carried out configuration-interaction calculations [16, 17, 24] using an octahedral MnS_6 cluster which includes explicitly the hybridization between the Mn $3d$ and the S $3p$ orbitals. We have set the hopping integrals for the e_g orbital at 1.92 eV and for the t_{2g} at 1.15 eV [24] and varied the energy difference between the d^5 and $d^6\underline{L}$ configurations (charge transfer energy Δ). Here $\underline{L}$ denotes the S $3p$ ligand hole states. The results are shown in Fig. 10.
Starting with the ionic calculation, we have in the ground state an electron occupation of 3.000 for the t_{2g} orbital and 2.000 for the e_g (values listed in the central panel). The corresponding ground state hole density is spherical (Fig. 10, left panel, red line), and the directional dependence of the low and high energy peaks in the calculated s-NIXS spectra follow (Fig. 10, two right panels) the t_{2g} (blue) and e_g (orange) orbital shapes, respectively, as we have seen already in Fig. 8. Switching on the hybridization between the d^5 and $d^6\underline{L}$ configurations, we can see that the electron occupation in the ground state increases with lowering the Δ values. It increases faster for the e_g than for the t_{2g} (values listed in the central panel), consistent with the fact that the hopping integral with the ligand is larger for the e_g than for the t_{2g}. In the strongly covalent case of $\Delta = 1$ eV we have 3.136 in the t_{2g} and 2.287 for the e_g. Accordingly, the ground state hole density, proportional to the NIXS signal, decreases for lower Δ values and becomes strongly non-spherical (left panel). This also means that the amount of hybridization can be

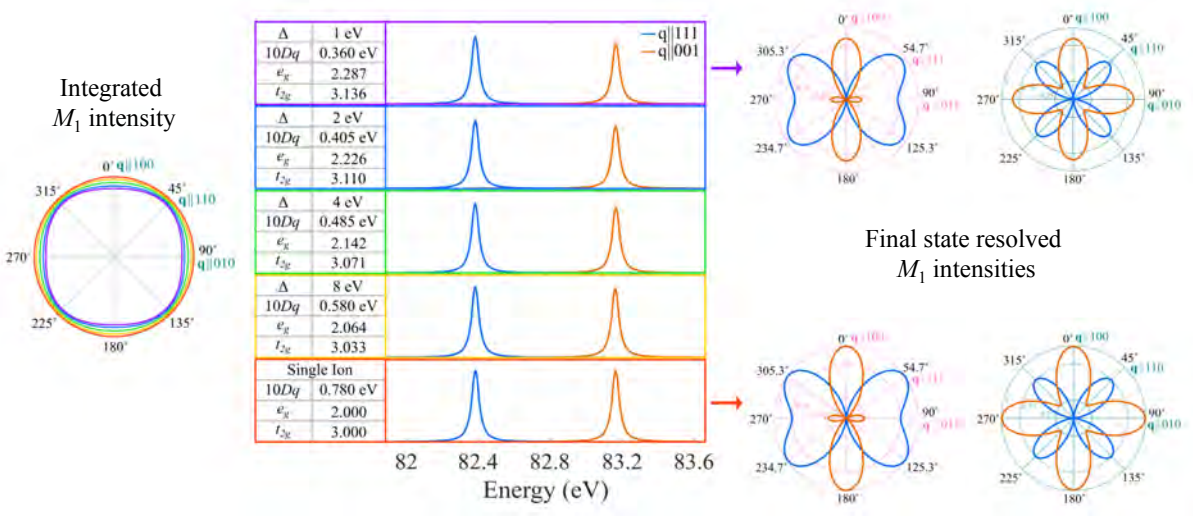

Fig. 10: *Mn M_1 simulations using a MnS_6 cluster calculated for various degrees of covalency. Left panel: Polar plot of the integrated intensity of the Mn M_1 in the [100] – [110] – [010] plane: from ionic (most outer circle) to strongly covalent (most inner distorted circle, Δ = 1 eV) case. Middle panel: Mn M_1 spectra along the $\vec{q}$ ∥ [100] (orange) and $\vec{q}$ ∥ [111] (blue) directions: from ionic (bottom curves) to strongly covalent (top curve, Δ = 1 eV). The Δ and corresponding ionic $10Dq$ values are indicated, together with the resulting e_g and t_{2g} occupation numbers. The energy splitting between the $\vec{q}$ ∥ [100] (orange) and $\vec{q}$ ∥ [111] (blue) peaks is fixed at 0.78 eV. Right panel: polar plot of the final state resolved Mn M_1 intensities (high energy peak in orange and low energy peak in blue), for the ionic (bottom) and strongly covalent (top, Δ = 1 eV) cases. Adapted from [3].*

extracted from the precise shape of the hole density as measured by s-NIXS.

Perhaps a surprising result is that the presence of hybridization does not have much influence on the s-NIXS spectrum, even for the $\Delta = 1\,\text{eV}$ case. It shows the same two peak structure, and the directional dependence of the low and high energy peaks still follows the t_{2g} (blue) and e_g (orange) orbital shapes, respectively. It may seem surprising that hybridization or covalency does little to the spectrum, but we can draw a parallel to x-ray absorption spectroscopy (XAS), which is also a core-level spectroscopy in which a core electron is excited into the valence shell. It is known that the $M_{4,5}$ edges of Ce and the $L_{2,3}$ of the $3d$ transition metal ions can be well reproduced using ionic calculations despite the fact that there is covalency. The reason is that the energy orderings of the electron configurations are identical in the initial state and in the XAS final state. Thus the spectral weights of the other local configurations are strongly suppressed due to quantum mechanical interference effects [16, 27]. Therefore, both XAS and NIXS, generally produce a spectrum that is very similar to the one that belongs to the main local configuration, e.g., the ionic configuration. Despite the fact that the overall s-NIXS spectrum is rather insensitive to hybridization, a closer look at the line shape and the intensities does reveal details that contain information about the hybridization strength. The middle panel of Fig. 10 show that the intensity of the high energy peak (e_g, orange) becomes smaller relative to that of the low energy peak (t_{2g}, blue) with decreasing Δ values. The s-NIXS spectrum can there-

fore be used to help determine quantitatively the parameter values describing the hybridization process.

In the ionic calculations, we have used a $10Dq$ value of 0.78 eV in order to get a separation of 0.78 eV between the two peaks in the Mn M_1 NIXS spectrum. We will name this the ionic-$10Dq$ parameter. Upon switching-on the hybridization, we must decrease the value of the ionic-$10Dq$ parameter in our calculations to maintain the 0.78 eV separation between the two peaks in the NIXS spectrum. A larger decrease is required when Δ gets smaller, i.e., when the hybridization gets stronger (see the values in the cental panel). This can be understood if one considers the fact that the hopping integral with the ligand is larger for e_g than for t_{2g}, and that the resulting difference in hybridization energy contributes to the energy splitting between the e_g bonding state and the t_{2g} equivalent. It is the combined effect of hybridization and the ionic-$10Dq$ that produces the 0.78 eV splitting in the NIXS spectrum, which we can define as the effective-$10Dq$. NIXS, like XAS, can thus provide direct access to the effective crystal field energy [16, 17, 28, 29]. The horizontal axis of the Sugano-Tanabe-Kamimura diagram presented in Fig. 5 can therefore be understood as the energy scale for the effective-$10Dq$ in covalent materials.

12 Metallic systems: ground state properties

The s-NIXS data presented so far concern insulating materials. We now will investigate the capabilities of this method for highly metallic systems. To this end, we have carried out measurements on elemental metals such as Cr, Fe, and Ni. For each metal we have used two single crystals, one having a surface with the (100) normal and the other the (111), in order to cover a sufficiently wide range of angles. All surfaces were epi-polished to mirror quality.

The results are shown in Fig. 11. The top panel displays the polar plot of the integrated M_1 intensities from scans collected from the (100) surface, and the middle panel from the (111) surface. The bottom panel summarizes the data in a 3-dimensional (3D) representation. Making use of the sum-rule argument explained above (since the quantities of concern are *integrated* intensities), we can assert that the images show the shape of the local $3d$ hole density of the metals in the ground state. We can clearly observe that there are significant differences between Cr, Fe, and Ni. These data can then be compared with *ab-initio* theoretical calculations in order to unveil to what extent electron correlation effects beyond mean field affect the ground state $3d$ charge density.

We would like to remark that information about the $3d$ charge density in highly metallic systems is in general very difficult to extract from spectroscopic data. In the presence of correlations, a quantitative analysis of the spectra is severely hampered by the large number of configurations that need to be included associated with the strong inter-site charge fluctuations. The use of *integrated* intensities in s-NIXS circumvents all these difficulties.

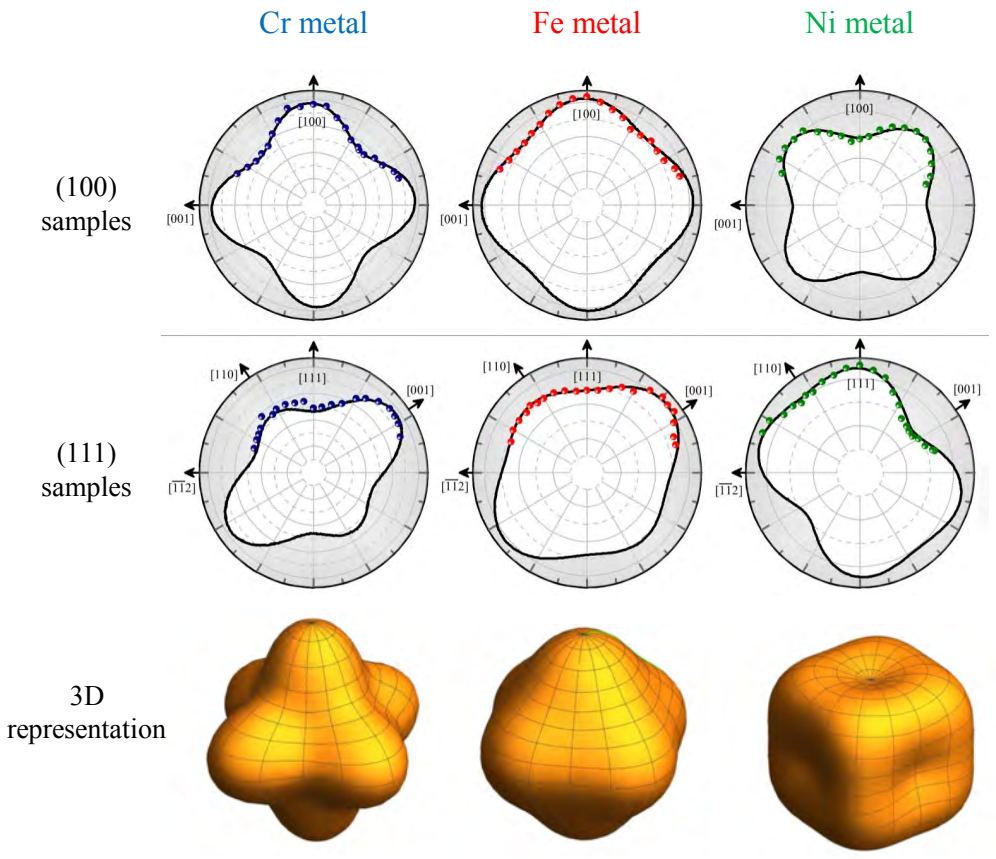

Fig. 11: *Shape of the hole density in the* 3d *shell of elemental Cr, Fe, and Ni metal. Top and middle panels: polar plots of the integrated intensity of the* M_1 *edge from the single crystal samples with the (100) and (111) surfaces, respectively. Bottom panel: a 3-dimensional representation of the measurement results.*

13 Concluding remarks

In conclusion, we have shown that s-NIXS has the unique ability to directly provide a spatial image of the local orbitals that are active in the formation of the ground state as well as of the excited states. This purely experimental method is especially valuable for tackling problems in complex systems where band formation and electron correlation effects are both important. s-NIXS can even provide direct information about the ground state properties of highly metallic systems, where spectroscopic techniques hit their limitations. The prospects of s-NIXS as a new experimental method need to be further explored. It is has, for example, the advantage that it is element-specific, and also allows for sophisticated sample environments, e.g., involving small samples, high pressures, and high/low temperatures.

Acknowledgements

The work presented in this chapter is the result of a fruitful and inspiring collaboration with M.W. Haverkort, M. Sundermann, H. Yavaş, H. Gretarsson, A. Amorese, B. Leedahl, K. Chen, M. Schmidt, H. Borrmann, Yu. Grin, and A. Severing.

References

[1] H. Yavaş, M. Sundermann, K. Chen, A. Amorese, A. Severing, H. Gretarsson, M.W. Haverkort, and L.H. Tjeng, Nat. Phys. **15**, 559 (2019)

[2] B. Leedahl, M. Sundermann, A. Amorese, A. Severing, H. Gretarsson, L. Zhang, A.C. Komarek, A. Maignan, M.W. Haverkort, and L.H. Tjeng, Nat. Commun. **10**, 5447 (2019)

[3] A. Amorese, B. Leedahl, M. Sundermann, H. Gretarsson, Z. Hu, H.-J. Lin, C.T. Chen, M. Schmidt, H. Borrmann, Yu. Grin, A. Severing, M.W. Haverkort, and L.H. Tjeng, Phys. Rev. X **11**, 011002 (2021)

[4] W. Schülke: *Electron Dynamics by Inelastic X-Ray Scattering* (Oxford University Press, 2007)

[5] M.W. Haverkort, A. Tanaka, L.H. Tjeng, and G.A. Sawatzky, Phys. Rev. Lett. **99**, 257401 (2007)

[6] R.A. Gordon, G.T. Seidler, T.T. Fister, M.W. Haverkort, G.A. Sawatzky, A. Tanaka, and T.K. Sham, EPL (Europhys. Lett.) **81**, 26004 (2008)

[7] R. Caciuffo, G. van der Laan, L. Simonelli, T. Vitova, C. Mazzoli, M.A. Denecke, and G.H. Lander, Phys. Rev. B **81**, 195104 (2010)

[8] M. Sundermann and M.W. Haverkort (unpublished)

[9] R.A. Gordon, M.W. Haverkort, S.S. Gupta, G.A. Sawatzky, J. Phys. Conf. Ser. **190**, 012047 (2009)

[10] J.A. Bradley, S.S. Gupta, G.T. Seidler, K.T. Moore, M.W. Haverkort, G.A. Sawatzky, S.D. Conradson, D.L. Clark, S.A. Kozimor, and K.S. Boland, Phys. Rev. B **81**, 193104 (2010)

[11] J.A. Bradley, K.T. Moore, G. van der Laan, J.P. Bradley, and R.A. Gordon, Phys. Rev. B **84**, 205105 (2011)

[12] T. Willers, F. Strigari, N. Hiraoka, Y.Q. Cai, M.W. Haverkort, K.-D. Tsuei, Y.F. Liao, S. Seiro, C. Geibel, F. Steglich, L.H. Tjeng, and A. Severing, Phys. Rev. Lett. **109**, 046401 (2012)

[13] M. Sundermann, M.W. Haverkort, S. Agrestini, A. Al-Zein, M. Moretti Sala, Y. Huang, M. Golden, A. de Visser, P. Thalmeier, L.H. Tjeng, and A. Severing, Proc. Nat. Acad. Science. U.S.A. **113**, 13989 (2016)

[14] M. Sundermann, H. Yavaş, K. Chen, D.J. Kim, Z. Fisk, D. Kasinathan, M.W. Haverkort, P. Thalmeier, A. Severing, and L.H. Tjeng, Phys. Rev. Lett. **120**, 016402 (2018)

[15] C.T. Chen, L.H. Tjeng, J. Kwo, H.L. Kao, P. Rudolf, F. Sette, and R.M. Fleming, Phys. Rev. Lett. **68**, 2543 (1992)

[16] F.M.F. de Groot, J. Electron Spectrosc. Relat. Phenom. **67**, 529 (1994)

[17] A. Tanaka and T. Jo, J. Phys. Soc. Jpn. textbf63, 2788 (1994)

[18] S.I. Csiszar, M.W. Haverkort, Z. Hu, A. Tanaka, H.H. Hsieh, H.-J. Lin, C.T. Chen, T. Hibma, and L.H. Tjeng, Phys. Rev. Lett. **95**, 187205 (2005)

[19] P. Hansmann, A. Severing, Z. Hu, M.W. Haverkort, C.F. Chang, S. Klein, A. Tanaka, H.H. Hsieh, H.-J. Lin, C.T. Chen, B. Fak, P. Lejay, and L.H. Tjeng, Phys. Rev. Lett. **100**, 066405 (2008)

[20] B.T. Thole, P. Carra, F. Sette, and G. van der Laan, Phys. Rev. Lett. **68**, 1943 (1992)

[21] P. Carra, B.T. Thole, M. Altarelli, and X. Wang, Phys. Rev. Lett. **70**, 694 (1993)

[22] C.T. Chen, Y.U. Idzerda, H.-J. Lin, N.V. Smith, G. Meigs, E. Chaban, G.H. Ho, E. Pellegrin, and F. Sette, Phys. Rev. Lett. **75**, 152 (1995)

[23] S. Sugano, Y. Tanabe, and H. Kamimura: *Multiplets of Transition-Metal Ions in Crystals* (Academic Press, New York, 1970)

[24] M.W. Haverkort, M. Zwierzycki, and O.K. Andersen, Phys. Rev. B **85**, 165113 (2012)

[25] R. Cowan: *The theory of atomic structure and spectra* (University of California, Berkeley, 1981)

[26] S. Blundell, *Magnetism in condensed matter* (Oxford University Press, 2001)

[27] O. Gunnarsson and K. Schönhammer, Phys. Rev. B **28**, 4315 (1983)

[28] S. Agrestini, Z. Hu, C.-Y. Kuo, M.W. Haverkort, K.-T. Ko, N. Hollmann, Q. Liu, E. Pellegrin, M. Valvidares, J. Herrero-Martin, P. Gargiani, P. Gegenwart, M. Schneider, S. Esser, A. Tanaka, A.C. Komarek, and L.H. Tjeng, Phys. Rev. B **91**, 075127 (2015)

[29] R.P. Wang, B. Liu, R.J. Green, M.U. Delgado-Jaime, M. Ghiasi, T. Schmitt, M.M. van Schooneveld, and F.M.F. de Groot, J. Phys. Chem. C **121**, 24919 (2017)